Chinese Journal of
POLYMER SCIENCE

RESEARCH ARTICLE

https://doi.org/10.1007/s10118-026-3889-x
Chinese J. Polym. Sci.

A Bottom-up United-atom Model for Polyethylene Chain Crystallization: a Potential Energy Matching Approach

Jing-Fu Shi[a], Di Song[b*], Lei Liu[a], and Chang-Qing Miao[a*]

[a] *National Key Laboratory of Science and Technology on Advanced Composites in Special Environment, Harbin Institute of Technology, Harbin 150001, China*
[b] *School of Mechanical and Electrical Engineering, University of Electronic Science and Technology of China, Chengdu 611731, China*

Abstract The elimination of explicit hydrogen degrees of freedom in the united-atom (UA) model leads to the loss of local bonded and non-bonded interactions, causing discrepancies in conformational predictions among different force fields and deviations from all-atom (AA) simulations. A bottom-up UA model was established to investigate polyethylene (PE) chain crystallization through potential energy matching. The optimized UA model successfully reproduced the single-chain crystallization characteristics with a predictive accuracy comparable to that of the optimized potentials for liquid simulations–all atom (OPLS-AA) force field. The potential energy evolution revealed that the enhanced dihedral torsional contribution in the optimized UA model compensated for the missing bond stretching and angle bending energies caused by the removal of hydrogen atoms, thereby maintaining the overall energy balance of the polymer chain. This study provides a bottom-up framework for developing transferable UA force fields and demonstrates the importance of energy consistency in multiscale polymer simulations.

Keywords United-atom model; Potential energy matching; Polyethylene

Citation: Shi, J. F.; Song, D.; Liu, L.; Miao, C. Q. A bottom-up united-atom model for polyethylene chain crystallization: a potential energy matching approach. *Chinese J. Polym. Sci*. https://doi.org/10.1007/s10118-026-3889-x

INTRODUCTION

Polyethylene (PE) is extensively employed in modern industries primarily because of its exceptional flexibility and adaptability in materials science.[1,2] The mechanical performance of PE can be readily tuned through molecular-level chemical design and control of its physical aggregation state.[3–5] The tunable performance allows it to be adapted for a wide range of applications, taking various product forms such as fibers, films, pipes, and packaging materials.[6–9]

The microscopic mechanisms of the mechanical behavior of PE have been explored using diverse experimental techniques. The evolution of molecular chains and aggregated structures can be investigated using neutron scattering,[10,11] infrared spectroscopy,[12,13] transmission electron microscopy,[14,15] atomic force microscopy,[16,17] and solid-state nuclear magnetic resonance spectroscopy.[18,19] Computational simulations such as molecular dynamics (MD),[20–23] Monte Carlo (MC),[24,25] and dissipative particle dynamics,[26,27] provide an effective approach for studying microscopic mechanisms at the molecular level. The atomistic modeling of PE primarily includes an all-atom (AA) model with explicit hydrogen atoms and a simplified coarse-grained (CG) model. In the CG model, multiple CH_n monomers are combined into a single bead,[28,29] whereas each CH_n monomer is treated as a single effective atom in the united-atom (UA) model.[30] The substitution of AA groups with a CG bead representation drastically reduces the number of degrees of freedom. Numerically, the CG model provides significant advantages by improving computational efficiency and enabling simulations to reach longer time and larger length scales.[31–35] In particular, the UA model simplifies CH_2 or CH_3 groups into a single bead to effectively capture the interactions and trajectories of the backbone, making it a promising approach to reproduce AA simulations.[36–38]

Various UA force fields, including OPLS-UA,[39] TraPPE-UA,[40] DREIDING II-UA[41] have been developed to study the physical and chemical properties of polymers. Although the functions and parameters of different force fields are obtained using diverse fitting approaches, including experimental data, ab initio molecular orbital calculations, and hybridization principles, they generally exhibit similar potential function forms.[39–43] However, the UA simulation results under different force fields are neither consistent with each other nor entirely in agreement with the AA simulations. It has been reported that neglecting the interactions between the hydrogen atoms attached to a carbon atom C_i and the atom C_{i+2} in the UA model results in differences in the folded structure of a single PE chain compared to the AA model.[44–48] The single PE chain folded into a regularly crystalline stem with the AA model of the OPLS-AA force field,[49] whereas it adopted disordered globular structures in the UA model. While the Forcite module of Material Studio has been used to fold an amorphous single chain into lamellar structures, it should be noted that the Forcite module lacks force-field parameters for

* Corresponding authors, E-mail: songdi@uestc.edu.cn (D.S.)
E-mail: miaocq@hit.edu.cn (C.Q.M.)
Received July 31, 2026; Accepted September 13, 2026; Published online November 18, 2026

© Chinese Chemical Society
Institute of Chemistry, Chinese Academy of Sciences

the UA model.[50,51] In addition, the chain folding and crystallization behavior under both isothermal and non-isothermal induced crystallization are significantly influenced by the choice of force fields in the UA model.[52]

To validate the AA and UA models, the stability of twin boundaries and slip in crystalline orthorhombic PE were investigated using density functional theory (DFT).[53] The DFT results were consistent with the OPLS-AA predictions and the available experimental data. The chain slip activation energies obtained from OPLS-AA were comparable to the DFT values, whereas systematically lower values were observed in the UA model. MD simulations using AA and UA models were performed to investigate the deformation mechanisms of semi-crystalline lamellar PE.[54] The AA model showed cavitation with limited chain slip and minor crystal reorientation, whereas the UA model predicted more extensive chain slip accompanied by pronounced crystal reorientation. These differences arise from the distinct parameterization strategies of UA force fields, which are often optimized for different target properties, and may therefore exhibit varying transferability in describing specific deformation processes.

To optimize the UA model, it has been suggested that adjusting the torsional barrier to compensate for intermolecular interactions induced by solvents or neighboring chains can lead to better agreement with the resultant lamellar dimensions.[55] The TraPPE-UA force field was improved by introducing improper torsional angle potentials, which enhanced the stereostructure and promoted crystallization and folding.[45,56–58] In the UA model, the potential of mean force was used to map explicit atoms onto UA potentials, providing functional forms that more accurately reflect the composite behavior of the UA sites.[59] In addition, an anisotropic united-atom (AUA) model has been proposed through the introduction of realistic anisotropic intermolecular potential functions or the simplification of UA bead mapping to the geometrical mean positions of the valence electrons.[60–64] It should be noted that the change in the mapped interaction centers of this model leads to variations in the mass distribution. Moreover, the top-down and bottom-up approaches in CG modeling provide valuable insights for optimizing the UA model.[65–72] The advent of machine learning has provided a new perspective for MD modeling. In particular, machine-learning potentials that combine DFT calculations and AA simulations have significantly enhanced the efficiency and accuracy of CG simulations.[73–77]

In this study, we developed a UA model based on OPLS-AA simulations, with the model investigated by integrating mapping center design and potential energy matching. The UA force fields obtained were validated through comparison with OPLS-AA simulations. Based on the energy evolution of chain folding and crystallization, a potential energy compensation strategy was proposed to evaluate and optimize the UA model.

THEORY AND METHODOLOGY

Mapping of Interaction Centers from AA Model to UA Model

In the UA model of PE, each CH_2 or CH_3 group is treated as a single-bead type. In most previous studies, the interaction centers were assigned to the carbon atom (C) positions in the mapping from the AA model to the UA model. As shown in Fig. 1, each UA bead was an isotropic interaction unit. In the CG model, the centers of mass (CM) are commonly used as interaction centers.[68] In the AUA model, the interaction centers are defined at the centers of the valence electrons (CVE), thereby introducing simplified anisotropy.[60] In this study, these interaction centers are mapped to assess the accuracy of the UA model. The mapping scheme is illustrated in Fig. 2.

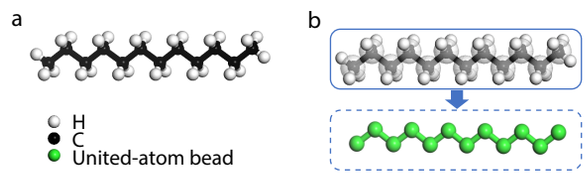


Fig. 1 Interaction centers mapped on carbon atoms. Hydrogen, carbon atoms and UA beads are depicted in white, black, and green, respectively. (a) AA model; (b) UA model.

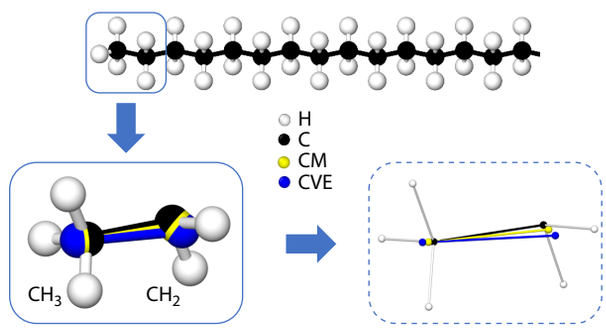


Fig. 2 Mapping scheme from AA model to UA model for CH_2 and CH_3 groups. White spheres represent hydrogen atoms (H), black spheres represent carbon atoms (C), yellow spheres represent centers of mass (CM), and blue spheres represent centers of valence electrons (CVE).

Several mapping consistency conditions must be satisfied in the UA model. The mass of UA bead k (M_k) is defined as the sum of the masses of its constituent hydrogen (m_k(H)) and carbon atoms (m_k(C)):

$$M_k = \sum_i m_k(\mathrm{H}_i) + m_k(\mathrm{C}) \tag{1}$$

The spatial coordinates of a UA bead k for the three mapped interaction centers, $\boldsymbol{R}_k^{\mathrm{C}}$, $\boldsymbol{R}_k^{\mathrm{CM}}$, and $\boldsymbol{R}_k^{\mathrm{CVE}}$:

$$\boldsymbol{R}_k^{\mathrm{C}} = \boldsymbol{r}_k(\mathrm{C}) \tag{2}$$

$$\boldsymbol{R}_k^{\mathrm{CM}} = \frac{\sum_i m_k(\mathrm{H}_i)\cdot \boldsymbol{r}_k(\mathrm{H}_i) + m_k(\mathrm{C})\cdot \boldsymbol{r}_k(\mathrm{C})}{\sum_i m_k(\mathrm{H}_i) + m_k(\mathrm{C})} \tag{3}$$

$$\boldsymbol{R}_k^{\mathrm{CVE}} = \frac{\sum_i v_k(\mathrm{H}_i)\cdot \boldsymbol{r}_k(\mathrm{H}_i) + v_k(\mathrm{C})\cdot \boldsymbol{r}_k(\mathrm{C})}{\sum_i v_k(\mathrm{H}_i) + v_k(\mathrm{C})} \tag{4}$$

where $\boldsymbol{r}_k$(H) and $\boldsymbol{r}_k$(C) are the coordinates of the hydrogen and carbon atoms in the AA model, which are mapped to the UA bead k. v_k(H) and v_k(C) represent the numbers of valence electrons of the hydrogen and carbon atoms, respectively.

UA Potential Energy Function

In the UA model, the interatomic potential energy E mainly comprises two contributing terms: bonded interactions E_{bonded}

and non-bonded interactions $E_{\text{non-bonded}}$. The bonded interactions consisted of bond length stretching E_{bond}, bond angle bending E_{angle} and dihedral angle torsion E_{dihedral}.

$$E = E_{\text{bonded}} + E_{\text{non-bonded}} \tag{5}$$

$$E_{\text{bonded}} = E_{\text{bond}} + E_{\text{angle}} + E_{\text{dihedral}} \tag{6}$$

E_{bond} and E_{angle} are expressed in classical harmonic forms, with K_b and K_θ denoting the energy constants, respectively, r and θ denote the bond length and bond angle, respectively, and r_0 and θ_0 representing the equilibrium bond length and bond angle, respectively. E_{dihedral} is expressed in multi-harmonic form, where the variable C_n is the energy constant. These constants were adjusted to ensure the local minimum of the dihedral potential in the *trans* (ϕ=180°) and *gauche* conformations (ϕ=60°, 300°).

$$E_{\text{bond}}(r) = \frac{1}{2}K_b\,(r - r_0)^2 \tag{7}$$

$$E_{\text{angle}}(\theta) = \frac{1}{2}K_\theta\,(\theta - \theta_0)^2 \tag{8}$$

$$E_{\text{dihedral}}(\phi) = \sum_{n=0}^{3} C_n\,(\cos\phi)^n \tag{9}$$

$E_{\text{non-bonded}}$ is described by the Lennard-Jones (LJ) 12-6 potential for van der Waals interactions within the cutoff distance r_c, where σ is the distance at zero energy and ε is the energy well depth.

$$E_{\text{non-bonded}}(r) = E_{\text{LJ}} = 4\varepsilon\left[\left(\frac{\sigma}{r}\right)^{12} - \left(\frac{\sigma}{r}\right)^{6}\right], \quad r \le r_c \tag{10}$$

Potential Energy Matching Algorithm

Based on the mapping consistency conditions from the AA model to the UA model, a matching condition was imposed to parameterize the potential function. Here, a potential energy matching approach is employed to determine the parameters, particularly the constant term C_0 in E_{dihedral}, whereas the atomic force obtained as the negative gradient of the potential energy does not explicitly include C_0. The potential energy matching condition between the UA model E_k^{UA} and the AA model E_k^{AA} is established for UA bead k:

$$E_k^{\text{UA}} = E_k^{\text{AA}} \tag{11}$$

E_k^{UA} is expressed as the corresponding contributing terms in Eqs. (5) and (6). E_k^{AA} is defined as the sum of the potential energies of the hydrogen and carbon atoms in the AA model, which are mapped to the UA bead k. The calculation of the individual potential energy terms follows the general conventions of MD, with the bonded interactions equally distributed to the corresponding atoms. For the UA bead k,

$$E_{\text{bond},k}^{\text{UA}} = \sum_{k\in\zeta_r} \frac{1}{2}E_{\text{bond}}(r) \tag{12}$$

$$E_{\text{angle},k}^{\text{UA}} = \sum_{k\in\zeta_\theta} \frac{1}{3}E_{\text{angle}}(\theta) \tag{13}$$

$$E_{\text{dihedral},k}^{\text{UA}} = \sum_{k\in\zeta_\phi} \frac{1}{4}E_{\text{dihedral}}(\phi) \tag{14}$$

where ζ_r, ζ_θ, and ζ_ϕ denote the sets of covalent bonds, bond angles, and dihedral angles, respectively. The interactions associated with k, $k \in \zeta_r$, $k \in \zeta_\theta$, $k \in \zeta_\phi$ contribute to individual potential energy terms. $E_{\text{non-bonded},k}^{\text{UA}}$ is the total van der Waals interaction between k and all neighboring beads within r_c.

$$E_{\text{non-bonded},k}^{\text{UA}} = \sum_{r_{kl}\le r_c} \frac{1}{2}E_{\text{non-bonded}}(r) \tag{15}$$

From the energy matching condition through Eq. (11), the loss function $f(E)_{\text{MSE}}$ is defined as the mean squared error of the potential energy:

$$f(E)_{\text{MSE}} = \frac{1}{N}\sum_{k=1}^{N}\left(E_k^{\text{AA}} - E_k^{\text{UA}}\right)^2 \tag{16}$$

Here, the losses of E_{bonded} and $E_{\text{non-bonded}}$ are minimized separately to reduce the interference between different energy terms.

$$f(E)_{\text{MSE}} = f(E_{\text{bonded}})_{\text{MSE}} + f(E_{\text{non-bonded}})_{\text{MSE}} \tag{17}$$

In this study, the loss function is minimized using the covariant matrix adaptation evolution strategy (CMA-ES) algorithm, a variant of the genetic algorithm.[78] To ensure physically reasonable optimization, the parameters of the UA model are constrained to physically meaningful ranges, leveraging the effectiveness of CMA-ES in searching for the global minimum of the parameter space. In the CMA-ES algorithm, the initial global step size was set to $\sigma^{(0)} = 0.1$.[79] The population sizes λ are set subject to the constraint $4 + 3\ln n \le \lambda \le 2n + 10$, where n denotes the number of parameters to be optimized.[80] For the bonded interaction optimization (n=6), population sizes of 10, 15 and 20 were tested, while population sizes of 7, 10 and 14 were examined for the non-bonded interaction optimization (n=2). Tests with different population sizes showed that the optimized parameters were essentially identical, whereas the population size only affected the convergence rate. Therefore, population sizes of 15 and 10 were selected for the bonded and non-bonded interaction optimizations, respectively. In the CMA-ES algorithm, the maximum number of generations was set to 1000, and the optimization was considered converged if the loss function varied by less than 1×10^{-6} within 100 generations.

MD Simulations of PE

To determine the parameters for the UA potential energy function, we performed AA simulations of the PE. All simulations were performed using an open-source parallel molecular dynamic code, Large-scale Atomic/Molecular Massively Parallel Simulator (LAMMPS).[81] In this study, the OPLS-AA force field[49] was used because it has been validated by DFT to accurately reproduce the crystalline characteristics and deformation mechanisms of PE.[49,53,54] We neglected electrostatics and assumed all atoms in the PE to be electrically neutral. This neutral-charge treatment is consistent with previous PE simulations using OPLS-AA, where the small partial charges of the C and H atoms are neglected because of the nonpolar nature of PE.[53,54] To avoid the influence of inconsistent 1–4 interaction parameters, additional 1–4 interactions were excluded in this work. These conventions are applied consistently in both AA and UA models, ensuring reproducible and compatible energy decomposition. We performed constant-temperature MD simulations of a single PE chain to obtain a dataset of atomic configurations and energies for the parameterization and optimization of the UA model.

To comprehensively sample the different chain conformations, PE chains of three lengths (100, 500, and 1000 carbon atoms) were simulated. The temperatures were set to 100, 300, and 500 K to capture the glass transition and melting be-

havior of the PE. The simulation systems were labeled according to chain length and temperature: a chain of 100 carbon atoms at 100 K was labeled as C100-100K, and a chain of 1000 carbon atoms at 500 K was labeled as C1000-500K. The temperature control in the simulation was achieved using a Nosé-Hoover thermostat.[82,83] In addition, the initial PE chain was constructed in an all-*trans* linear geometry and placed in a cubic simulation box with periodic boundary conditions. The box length was set to twice the end-to-end distance (R_{ee}) of the initial chain, which exceeds 4–5 times its radius of gyration (R_g) to fully accommodate it.[84] The integration time step was set as 1 fs. The simulation process consists of two main steps. First, the PE chain was simulated for 100 ps using an NVT ensemble. Second, the simulation was continued for 10 ns to generate the chain trajectories for data extraction.

RESULTS AND DISCUSSION

Autocorrelation and Subsampling of Chain Trajectories

To enhance the efficiency of the potential energy-matching algorithm, subsampled trajectories were identified using an autocorrelation analysis.[85–88] The R_{ee} and R_g characterize chain extension and spatial distribution and serve to analyze temporal correlations in chain dynamics. For a given observable f (*e.g.*, R_{ee} or R_g), the normalized autocorrelation function (ACF) can be estimated for a finite set of N_S samples as

$$\mathrm{ACF}(t) = \frac{\frac{1}{N_S - t}\sum_{n=1}^{N_S - t}(f_n - \mu_f)(f_{n+t} - \mu_f)}{\frac{1}{N_S}\sum_{n=1}^{N_S}(f_n - \mu_f)^2} \tag{18}$$

where μ_f is the mean value of the observable f,

$$\mu_f = \frac{1}{N_s}\sum_{n=1}^{N_s} f_n \tag{19}$$

Based on the normalized autocorrelation function, the integrated autocorrelation time (τ_{int}) is given by

$$\tau_{int} = \Delta t\left(1 + 2\sum_{1}^{M}\mathrm{ACF}(t)\right) \tag{20}$$

where Δt denotes the sampling time step and M denotes the maximum lag. The effective sample size (N_{eff}) was derived from ACF.

$$N_{eff} = \frac{N_s \Delta t}{2\tau_{int}} \tag{21}$$

Fig. 3 shows the normalized ACF of R_{ee} and R_g for the PE chain of C1000 at different temperatures, which illustrates the temporal correlations of these observables along the simulation trajectories. The normalized ACF of each observable gradually decays from 1 as the time lag increases, and eventually reaches zero. The lag at which the ACF crosses zero represents the correlation time, after which R_{ee} or R_g is effectively uncorrelated. In Fig. 3(a), the time lag of R_{ee} remains below 0.5 ns at different temperatures. In contrast, in Fig. 3(b), the time lag of R_g at the low temperature of 100 K exceeds 0.5 ns, which is longer than at other temperatures. Longer time lags led to a decrease in the effective sample size.

N_{eff} obtained from Eq. (21), based on the autocorrelation analysis of R_{ee} and R_g for all simulation systems, is depicted in Fig. 4. The values of N_{eff} reflect the sensitivity of R_{ee} and R_g to the chain dynamics. It can be observed that at a high temperature of 500 K for different systems, N_{eff} reaches its largest value. This can be attributed to the enhanced atomic motion at higher temperatures, which induces more frequent conformational changes and consequently reduces the correlation. Specifically, the minimum N_{eff} obtained from R_{ee} is 8.9 for the C500-300K system in Fig. 4(a), where as the minimum N_{eff} obtained from R_g is 5.2 for the C100-300K system in Fig. 4(b). These differences are expected, as R_{ee} primarily captures the overall chain extension, whereas R_g characterizes the spatial distribution of monomers, making the two quantities differently responsive to chain dynamics. To ensure statistical independence of the chain trajectories, five evenly spaced samples were taken from the 10 ns simulation of each system, using the minimum N_{eff} (5.2) as a reference. A total of 45 trajectory files comprising 24000 carbon atoms were obtained for the potential energy matching study.

Parameterization of the UA Model

The UA force fields obtained by potential energy matching to C, CM, and CVE are designated as PEM-C-UA, PEM-CM-UA, and PEM-CVE-UA, respectively. The parameters were optimized using the CMA-ES algorithm within physically reasonable search ranges, which were defined based on the parameters reported in OPLS-AA and conventional UA force fields. The bond stretching force constant (K_b), angle bending force constant (K_θ), and dihedral torsional coefficient (C_n) were constrained within 0–2000 kcal/mol/Å^2, 0–2000 kcal/mol/rad^2, and 10–20 kcal/mol, respectively. The LJ energy well depth (ε) and distance parameter (σ) were constrained to 0–1 kcal/mol and 0–10 Å, respectively. The cutoff distance r_c for $E_{non\text{-}bonded}$ must first be defined for the parameterization of the UA force fields. For the LJ potential,

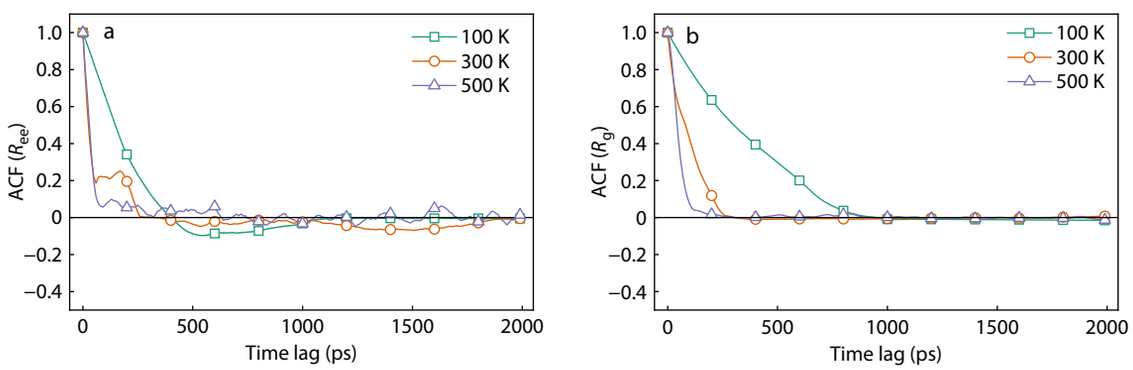


Fig. 3 Time evolution of the normalized autocorrelation function (ACF) of (a) R_{ee} and (b) R_g as a function of time lag.

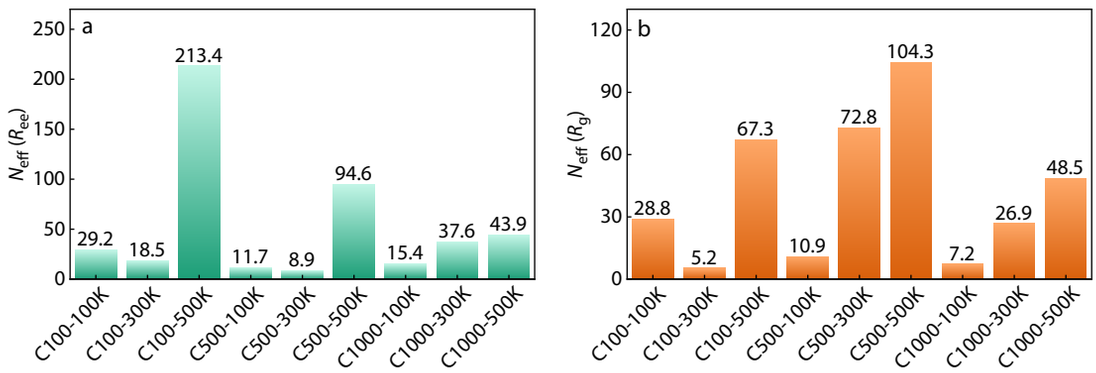


Fig. 4 Effective sample size (N_{eff}) of chain trajectories of simulation systems with different chain lengths and temperatures, calculated using: (a) R_{ee}, (b) R_g.

r_c is typically set as a multiple of the distance at zero energy, σ, that is, $r_c = \alpha\sigma$.

Fig. 5 presents the final loss of $E_{non\text{-}bonded}$ derived from different mapped interaction centers at various cutoff distances, with α ranging from 1.5 to 5.0. The final loss decreased with increasing α, and the reduction became marginal for α>2.5. Considering that the computational cost of the non-bonded interactions scales approximately as r_c^3, α=2.5 is chosen to balance accuracy and efficiency.

Fig. 6 shows the evolution of the loss function during iterative optimization for E_{bonded} and $E_{non\text{-}bonded}$ in different force fields derived from various mapped interaction centers. For all force fields, the loss decreases over successive generations and ultimately reaches a stable value, indicating the convergence of the optimization. As shown in Fig. 6(a), the final loss of E_{bonded} for the PEM-C-UA force field, which uses carbon atoms as the mapped interaction centers, is approximately 2.881, which is lower than that of the other two force fields. Similarly, in Fig. 6(b), the loss of $E_{non\text{-}bonded}$ for the PEM-C-UA is the lowest at approximately 0.702, indicating that the PEM-C-UA achieves the best agreement with the target potential energies among the three force fields.

Upon the convergence of the potential energy loss, the resulting optimal parameters were considered as the target values. Table 1 presents the force field parameters, including those for E_{bonded} and $E_{non\text{-}bonded}$, along with r_c applied for the non-bonded interactions. Based on these parameters, we compared several conventional UA force fields (OPLS-UA, TraPPE-UA, and DREIDING II-UA) with the force fields developed in this work *via* potential energy matching, as illustrated in Fig. 7.

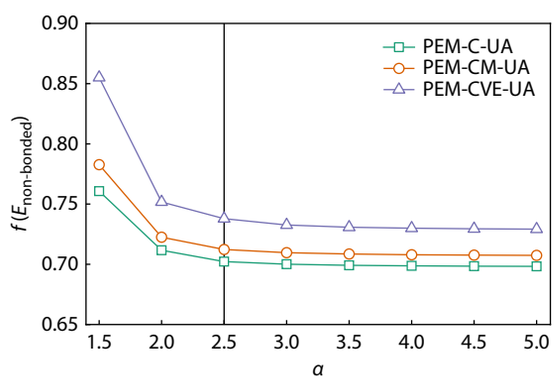


Fig. 5 Final loss of $E_{non\text{-}bonded}$ for force fields derived from different mapped interaction centers at various cutoff distances $r_c = \alpha\sigma$.

In Fig. 7(a), the equilibrium bond lengths r_0 of PEM-CM-UA and PEM-CVE-UA are significantly longer than those of the other force fields, reflecting the displacement of the mapping interaction centers from the backbone carbon atoms. Consequently, the equilibrium bond angles θ_0 of PEM-CM-UA and PEM-CVE-UA were smaller than those of the other force fields, as illustrated in Fig. 7(b). The energy constant k_θ in PEM-CVE-UA is relatively low, allowing greater bond angle deviations and more flexible chain segments. In contrast, k_θ in PEM-C-UA was larger, leading to stiffer chain segments.

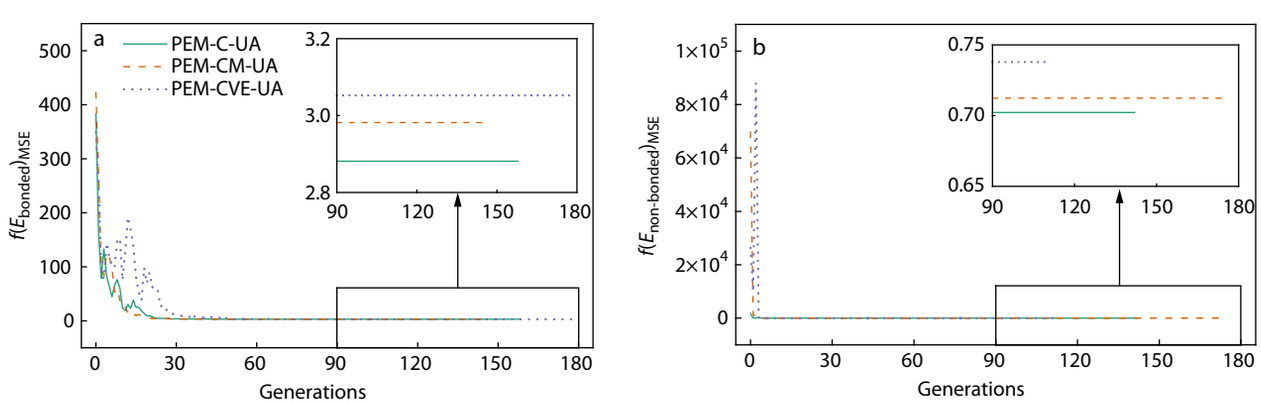


Fig. 6 Iterative evolution of the loss function for force fields derived from different mapped interaction centers: (a) E_{bonded}, (b) $E_{non\text{-}bonded}$.

https://doi.org/10.1007/s10118-026-3889-x

Table 1 Parameters of force fields derived from different mapped interaction centers for the UA model.

Force field	K_b (kcal/mol/Å^2)	r_0 (Å)	K_θ (kcal/mol/rad^2)	θ_0 (°)	C_0 (kcal/mol)	C_1 (kcal/mol)	C_2 (kcal/mol)	C_3 (kcal/mol)	ε (kcal/mol)	σ (Å)	r_c (Å)
PEM-C-UA	506.662	1.531	209.948	112.515	6.011	−5.753	0.277	10.095	0.13433	3.683	9.2
PEM-CM-UA	524.318	1.640	111.436	102.713	6.084	−6.961	−0.416	10.575	0.14904	3.603	9.0
PEM-CVE-UA	385.024	1.802	20.046	89.465	6.279	−7.045	−0.096	11.040	0.19455	3.393	8.5

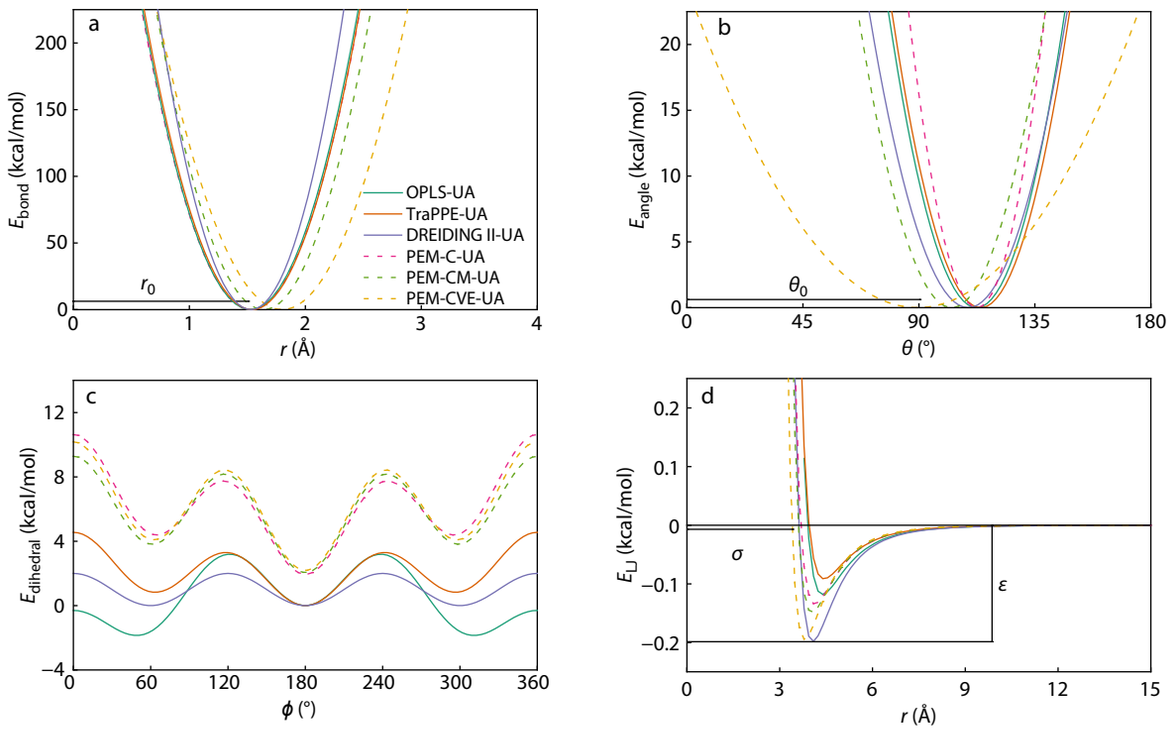


Fig. 7 Potential energy profiles for the UA model, comparing conventional force fields (OPLS-UA, TraPPE-UA, DREIDING II-UA) and force fields derived from potential energy matching (PEM-C-UA, PEM-CM-UA, PEM-CVE-UA). (a) E_{bonded}, (b) E_{angle}, (c) $E_{dihedral}$, (d) $E_{non\text{-}bonded}$.

In Fig. 7(c), the potential energy profiles of the dihedral angle torsion interactions for the force fields developed in this study are significantly higher than those of the conventional force fields. This leads to higher torsional energy barriers for dihedral rotation, which is consistent with literature reports that enhancing the role of hydrogen atoms improves the optimization of conventional UA force fields.[45,55] In Fig. 7(d), the distance at zero energy σ of PEM-CVE-UA is smaller than that of the other force fields, which shortens the equilibrium distance and may result in more compact chain segments. The van der Waals interaction profiles of PEM-C-UA and PEM-CM-UA fall between those of conventional force fields.

Validation of the UA Model

To validate the potential energy-matching force fields, we benchmarked their performance against the conventional UA force fields. Specifically, we calculated E_{bonded} and $E_{non\text{-}bonded}$ of an independent test set consisting of 27 chain trajectory files using OPLS-AA, comprising a total of 14400 carbon atoms. These values were then used as references to evaluate the predictions of the various UA force fields. Fig. 8 presents a comparison of E_{bonded} predicted by various UA force fields with those calculated using OPLS-AA. The diagonal dashed line indicates perfect agreement between the two force fields. The root-mean-square error (RMSE) was computed for each trajectory in the independent test set and the reported value was the mean across the chain trajectories. The confidence interval (95% CI) was estimated by bootstrap resampling over the chain trajectories.

In Figs. 8(a)–8(c), E_{bonded} predicted by conventional UA force fields are clearly distributed below the diagonal, indicating a systematic underestimation relative to the OPLS-AA reference values. In contrast, E_{bonded} predicted by the potential energy matching force fields (Figs. 8d–8f) are clustered around the diagonal, demonstrating significantly improved agreement with the reference values. The RMSEs of E_{bonded} predicted by the potential energy-matching force fields were lower than those predicted by the conventional UA force fields. In particular, PEM-C-UA achieved the lowest RMSE of 1.357 kcal/mol (95% CI: 1.214–1.494 kcal/mol), whereas that of TraPPE-UA was 3.188 kcal/mol (95% CI: 2.738–3.580 kcal/mol).

Fig. 9 illustrates $E_{non\text{-}bonded}$ predicted by various UA force fields compared with the corresponding values calculated using the OPLS-AA force field. $E_{non\text{-}bonded}$ predicted by all UA force fields are largely clustered around the diagonal. Among the force fields, PEM-C-UA exhibited the lowest RMSE of 0.481 kcal/mol (95% CI: 0.417–0.549 kcal/mol), whereas the RMSE of TraPPE-UA was 0.591 kcal/mol (95% CI: 0.507–0.685 kcal/mol).

The predictive performance of each force field was further evaluated based on the statistical results of the bonded and non-bonded potential energies. Table 2 summarizes the

https://doi.org/10.1007/s10118-026-3889-x

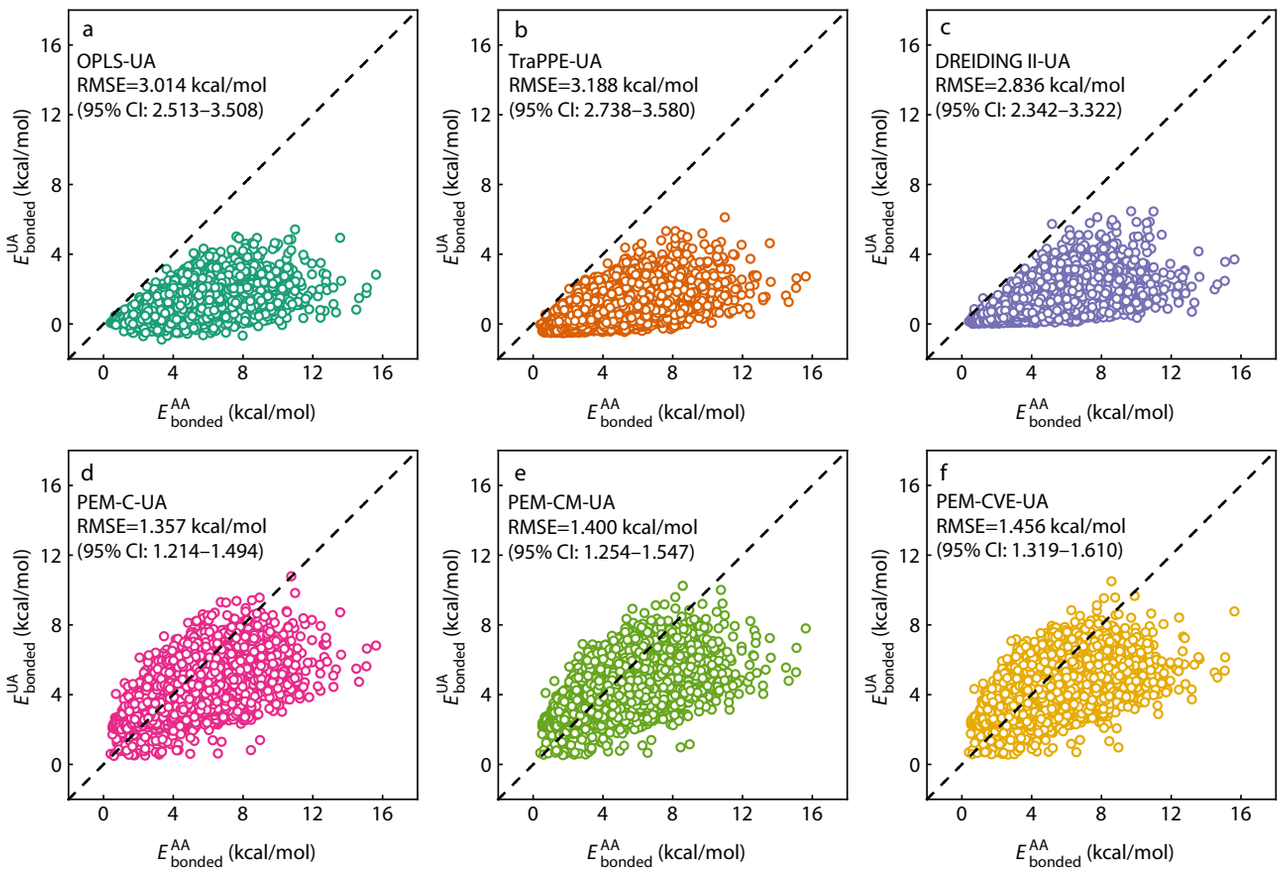


Fig. 8 E_{bonded} of 14400 carbon atoms across 27 trajectory files predicted by various UA force fields compared with OPLS-AA reference values. (a) OPLS-UA, (b) TraPPE-UA, (c) DREIDING II-UA, (d) PEM-C-UA, (e) PEM-CM-UA, (f) PEM-CVE-UA.

mean-square errors (MSEs) and coefficients of determination (R^2) for E_{bonded} and $E_{non\text{-}bonded}$, as predicted by various force fields on an independent test set. R^2 quantifies how accurately the UA force fields reproduce the variation in the reference energies, with values closer to 1 indicating a higher degree of agreement,[89,90] as defined by

$$R^2 = 1 - \frac{\sum_{k=1}^{N}\left(E_k^{AA} - E_k^{UA}\right)^2}{\sum_{k=1}^{N}\left(E_k^{AA} - \bar{E}^{AA}\right)^2} \quad (22)$$

where $\bar{E}^{AA}$ is the mean potential energy calculated in the AA model.

In Table 2, the MSEs of E_{bonded} predicted by PEM-C-UA, PEM-CM-UA, and PEM-CVE-UA are notably smaller than those of the conventional force fields. TraPPE-UA exhibited the largest errors, whereas PEM-C-UA exhibited the smallest errors. The conventional force fields exhibited R^2 values below zero, whereas the potential energy-matching force fields yielded R^2 values above zero. Among all force fields, PEM-C-UA exhibited the highest R^2 of 0.509. Although this value is less than 1, it corresponds to a positive R^2 and indicates a substantial improvement over conventional force fields. The MSEs of $E_{non\text{-}bonded}$ show a slight improvement, with PEM-C-UA achieving the lowest values. PEM-C-UA also exhibited the highest R^2 value (0.730). Overall, PEM-C-UA captured approximately 50% of the variance in E_{bonded}. The bonded energy distributions were further analyzed to distinguish systematic deviations from statistical fluctuations. The average bonded energies obtained from OPLS-AA and PEM-C-UA were 3.813 and 3.560 kcal/mol, respectively, corresponding to a difference of only 0.253 kcal/mol, whereas the standard deviations of the energy fluctuations were 2.037 and 1.299 kcal/mol, respectively. Therefore, the fluctuation amplitudes are much larger than the systematic deviation between the two models, indicating that the moderate correlation coefficient is mainly associated with intrinsic thermal fluctuations during the MD simulations rather than significant deviations in the averaged bonded energy. Considering the inherent complexity of MD systems and the dominant contribution of thermal fluctuations to instantaneous energy variations, this level of agreement was considered reasonable.

Compared with conventional force fields, the potential energy matching force fields generally achieve enhanced predictions of potential energies, with significant improvements observed for E_{bonded}. Specifically, the PEM-C-UA force field, using carbon atoms as the mapping centers, exhibited a minimal error in predicting both E_{bonded} and $E_{non\text{-}bonded}$. This supports the rationality of constructing a UA model with carbon atoms as the mapping interaction centers from the perspective of the potential energy.

Chain Crystallization under Different Force Fields

Based on the validation of the UA model, molecular dynamics simulations of PE chain crystallization were carried out using

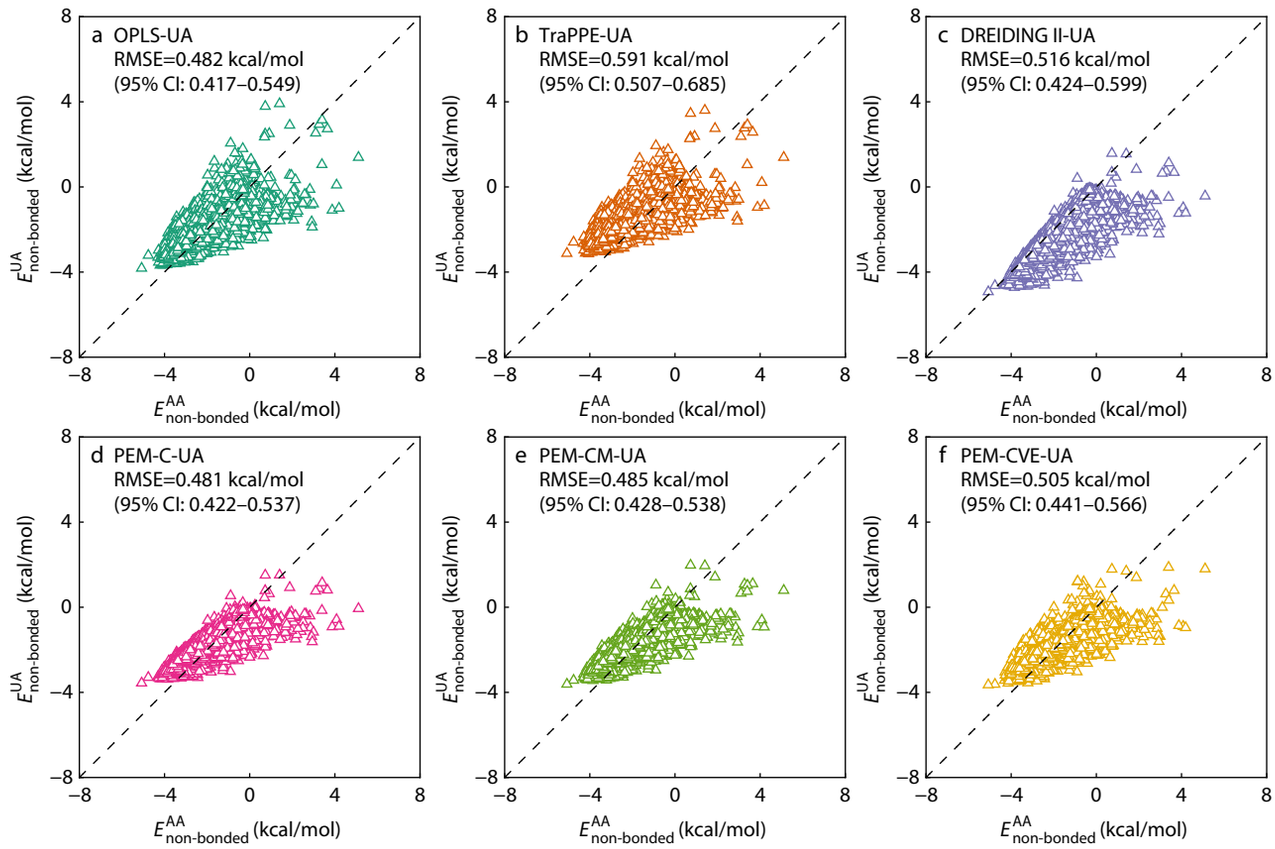


Fig. 9 $E_{non\text{-}bonded}$ of 14400 carbon atoms across 27 trajectory files predicted by various UA force fields compared with OPLS-AA reference values. (a) OPLS-UA, (b) TraPPE-UA, (c) DREIDING II-UA, (d) PEM-C-UA, (e) PEM-CM-UA, (f) PEM-CVE-UA.

Table 2 MSE and R^2 of E_{bonded} and $E_{non\text{-}bonded}$ for different force fields.

Force field	E_{bonded}		$E_{non\text{-}bonded}$	
	MSE	R^2	MSE	R^2
OPLS-UA	11.728	−1.826	0.316	0.708
TraPPE-UA	12.502	−2.012	0.526	0.513
DREIDING II-UA	10.441	−1.516	0.358	0.669
PEM-C-UA	2.038	0.509	0.292	0.730
PEM-CM-UA	2.150	0.482	0.299	0.723
PEM-CVE-UA	2.321	0.441	0.325	0.699

various force fields. AA simulations employed the OPLS-AA force field, whereas the UA simulations used the six force fields described above. Single PE chains containing 500 and 2000 carbon atoms (C500 and C2000) were examined to further assess the applicability and scalability of the potential energy-matching force fields. The linear chain was first simulated for 1 ns at 600 K under the NVT ensemble to allow full collapse and folding into a molten random coil. The chain was then cooled to induce crystallization *via* both isothermal and non-isothermal protocols. For isothermal crystallization (IC), the temperature was set to 300 K and the simulation was run for 5 ns. For non-isothermal crystallization (NIC), the chain was quenched from 600 K to 300 K at a cooling rate of 100 K/ns. Each system was independently simulated thrice.

To characterize the microstructure metrics of the PE melt, the distributions of the bond lengths and angles were averaged over three independent simulations. In the AA model, the bond lengths and angles correspond to the C—C and C—C—C angles, which reflect the backbone conformation. In the UA model, the bond lengths and angles correspond to the CH_2—CH_2 (CH_3) and CH_2—CH_2—CH_2 (CH_3) angles of the mapped beads. The distributions of the bond lengths and angles for chains of different lengths, fitted using Gaussian functions, are shown in Fig. 10.

In Fig. 10(a), the bond-length distribution curves of the C500 PE chain obtained with the UA force fields are generally similar to the curve of OPLS-AA, except for the rightward shift observed in PEM-CM-UA and PEM-CVE-UA. These deviations are expected: in PEM-CM-UA, the bond lengths correspond to the distances between the centers of mass, while in PEM-CVE-UA, they correspond to the distances between centers of valence electrons. In Fig. 10(b), the bond angle distribution curve of PEM-C-UA closely resembles that of the OPLS-AA in terms of distribution width and peak shape. Among all UA

https://doi.org/10.1007/s10118-026-3889-x

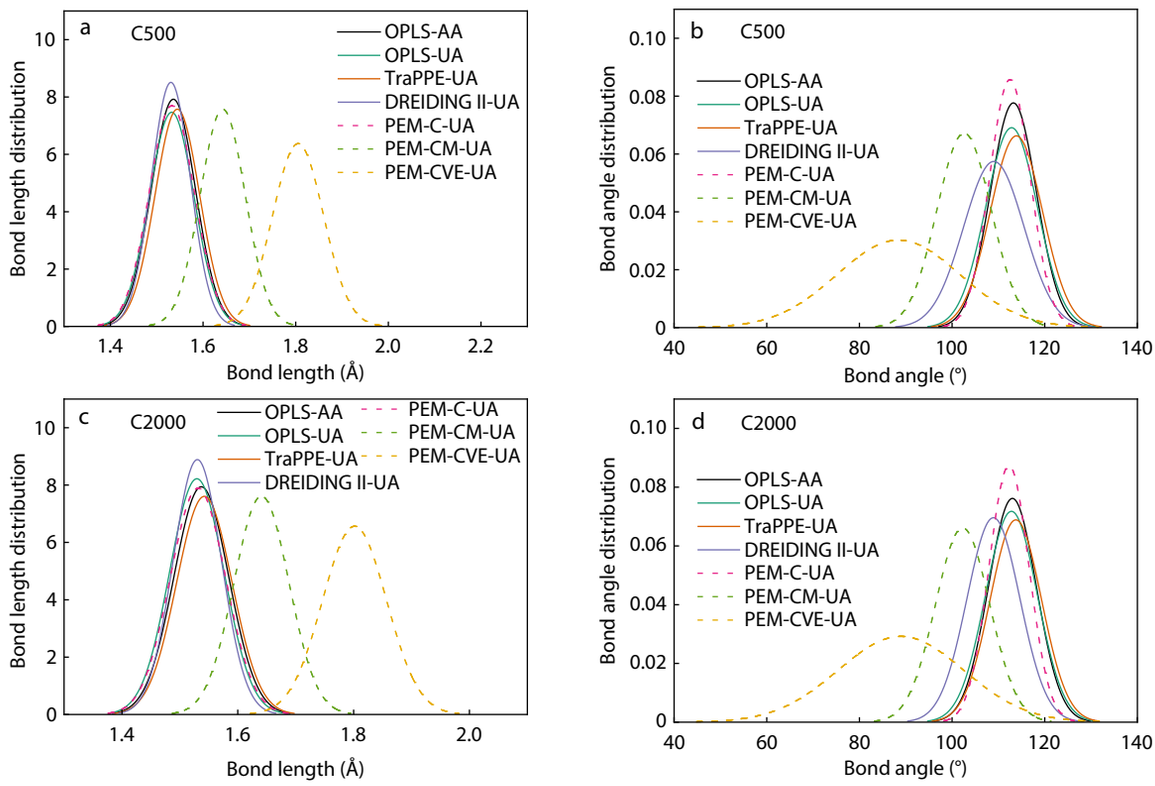


Fig. 10 Microstructure metrics of molten PE chains at 600 K under different force fields: (a) bond length distribution of C500, (b) bond angle distribution of C500, (c) bond length distribution of C2000, (d) bond angle distribution of C2000.

force fields with carbon atoms as the mapping centers, the peak of the DREIDING II-UA distribution is noticeably lower than that of the OPLS-AA. The bond angle distribution curves of PEM-CM-UA and PEM-CVE-UA exhibit a leftward shift relative to the OPLS-AA curve. In particular, the distribution curve of PEM-CVE-UA is lower and broader, indicating a wider distribution of bond angles.

In Figs. 10(c) and 10(d), the bond length and bond angle distributions of C2000 obtained with various force fields exhibit distribution patterns similar to those of C500. The distribution curves of PEM-CM-UA and PEM-CVE-UA exhibited similar shifts. In Fig. 10(d), the bond angle distribution of PEM-C-UA exhibited the most pronounced peak, indicating that its bond angles are more narrowly distributed around the mean value.

The crystallization of molten PE chains occurs under both isothermal and non-isothermal conditions. To characterize the structural evolution during crystallization, the crystallinity, X_c, was evaluated using the site order parameter (SOP).[91] The SOP of atom k is given by

$$\mathrm{SOP}_k = \frac{3}{2}\left\langle \left(\mathbf{e}_i \cdot \mathbf{e}_j\right)^2 \right\rangle_R - \frac{1}{2} \tag{23}$$

where $\mathbf{e}_i$ and $\mathbf{e}_j$ denote the vectors of any two atoms i and j determined from the positions of the bonded neighboring atoms ($\mathbf{e}_i = (x_{i+1}\text{-}x_{i-1}, y_{i+1}\text{-}y_{i-1}, z_{i+1}\text{-}z_{i-1})$, $\mathbf{e}_j = (x_{j+1}\text{-}x_{j-1}, y_{j+1}\text{-}y_{j-1}, z_{j+1}\text{-}z_{j-1})$). The neighboring atoms were identified from the list of bonded atoms along the PE chain. The chain-end atoms were excluded from the SOP calculations because one of their bond vectors was missing. The critical order of the SOP was set to 0.7, to distinguish between the crystalline and noncrystalline phases and to calculate the crystallinity.

Fig. 11 shows the X_c curves of C500 and C2000 under various force fields during isothermal and non-isothermal crystallization. The X_c values represent the averages of three independent simulations. As shown in Fig. 11(a), the X_c of C500 increases significantly under OPLS-AA. The X_c curve under PEM-C-UA is slightly lower than that under OPLS-AA, whereas the X_c curves obtained under the other UA force fields are much lower. In Fig. 11(b), the X_c curves of C2000 under various force fields exhibit features similar to those shown in Fig. 11(a). The X_c curve under the PEM-C-UA was slightly higher than that under the OPLS-AA force field. The two curves partially overlapped, and PEM-C-UA provided improved accuracy. The X_c curves during IC indicate that crystallization occurs synchronously under both PEM-C-UA and OPLS-AA, which is governed by low temperature. In Figs. 11(c) and 11(d), the X_c of PE chains with different lengths increases significantly under OPLS-AA and PEM-C-UA, while it remains lower under other UA force fields. Crystallization occurred earlier under PEM-C-UA than under OPLS-AA during NIC. The faster crystallization in the UA model is primarily due to the higher mobility of the chain segments, which is facilitated by neglecting hydrogen atoms.

Snapshots of the folded chains in Fig. 12 correspond to the final crystallinity, as shown in Fig. 11. The proportion of *trans* conformation P_m along the backbone of the PE chains was computed to quantify the distribution of *trans* conformations in the folded structures. The *trans* state was defined as a dihedral angle within 180°±15°.[92] It can be seen that the AA chains of both C500 and C2000 form regularly folded stems

https://doi.org/10.1007/s10118-026-3889-x

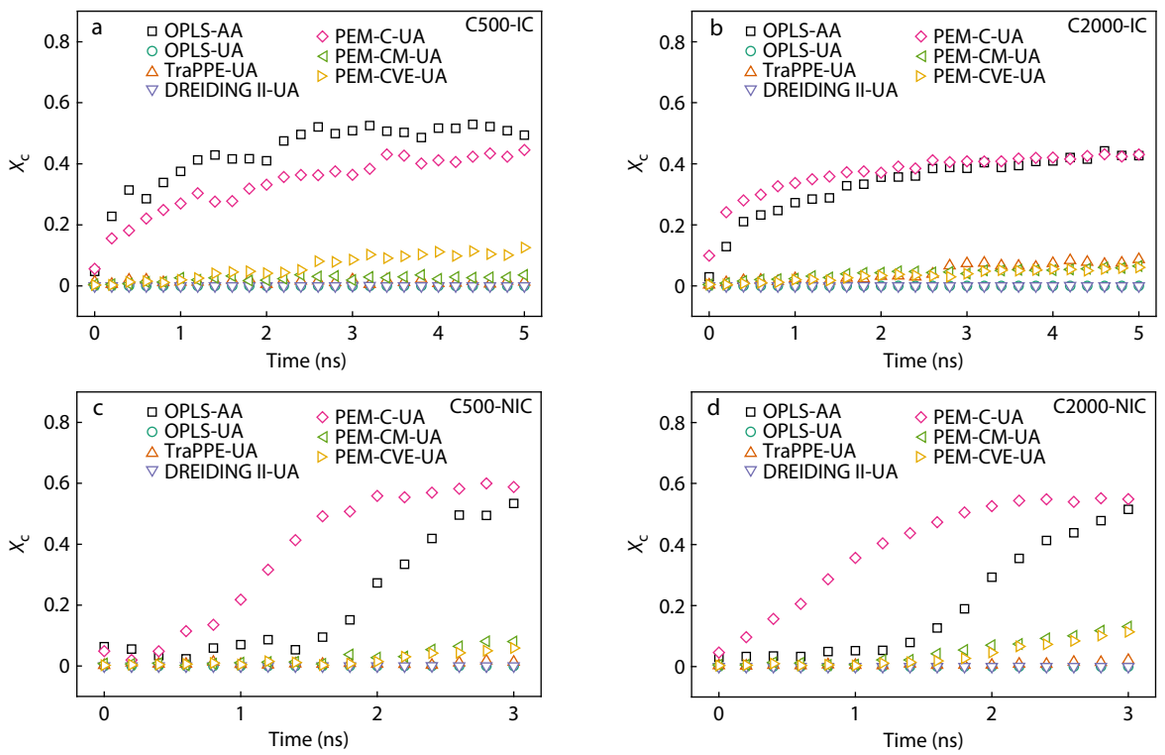


Fig. 11 Time evolution of X_c during isothermal and non-isothermal crystallization under different force fields. (a) C500-IC, (b) C2000-IC, (c) C500-NIC, (d) C2000-NIC.

Force field	OPLS-AA	OPLS-UA	TraPPE-UA	DREIDING II-UA	PEM-C-UA	PEM-CM-UA	PEM-CVE-UA
C500-IC	X_c=0.494 P_m=0.668	X_c=0.000 P_m=0.265	X_c=0.013 P_m=0.517	X_c=0.000 P_m=0.366	X_c=0.445 P_m=0.785	X_c=0.035 P_m=0.726	X_c=0.125 P_m=0.800
C2000-IC	X_c=0.427 P_m=0.677	X_c=0.000 P_m=0.265	X_c=0.087 P_m=0.569	X_c=0.000 P_m=0.355	X_c=0.430 P_m=0.799	X_c=0.065 P_m=0.732	X_c=0.061 P_m=0.779
C500-NIC	X_c=0.534 P_m=0.689	X_c=0.000 P_m=0.273	X_c=0.013 P_m=0.555	X_c=0.000 P_m=0.355	X_c=0.588 P_m=0.810	X_c=0.080 P_m=0.665	X_c=0.059 P_m=0.761
C2000-NIC	X_c=0.515 P_m=0.702	X_c=0.000 P_m=0.276	X_c=0.205 P_m=0.552	X_c=0.000 P_m=0.362	X_c=0.549 P_m=0.815	X_c=0.131 P_m=0.748	X_c=0.113 P_m=0.785

Fig. 12 Snapshots of folded chains under different force fields and crystallization conditions. Folded chains are colored differently to distinguish different force fields: yellow for OPLS-AA, blue for conventional UA force fields, and green for the UA force fields developed in this work. X_c denotes the crystallinity of the folded structure, while P_m represents the proportion of *trans* conformations.

under OPLS-AA. All UA chains remained as disordered globular folded structures under the three conventional UA force fields. In contrast, under the PEM-C-UA developed in this study, chains formed regularly folded stems, whereas disordered globular folded structures were observed under both PEM-CM-UA and PEM-CVE-UA. This demonstrates that PEM-C-UA can successfully reproduce the folding and crystallization of PE chains, exhibiting accuracy and reliability in good agreement with those of the OPLS-AA. It should be noted that a larger value of P_m indicates an enrichment of *trans* conformations in the folded structure but does not imply higher crystallinity or the formation of regularly folded stems. For OPLS-

https://doi.org/10.1007/s10118-026-3889-x

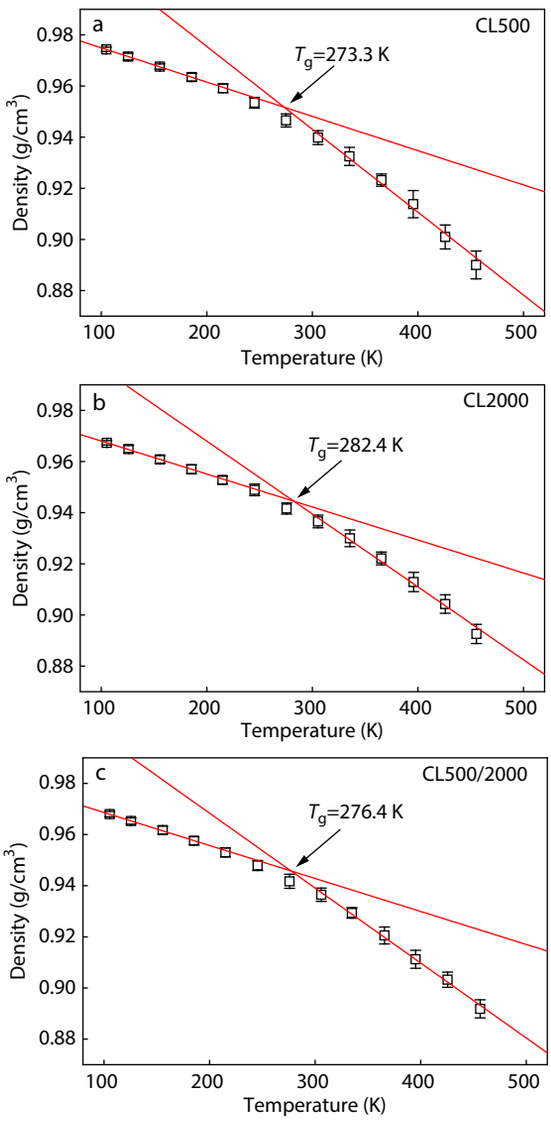


Fig. 13 Density evolution with temperature for different multi-chain systems and determination of glass transition temperature (T_g) using PEM-C-UA: (a) CL500, (b) CL2000, (c) CL500/2000.

AA and PEM-C-UA, a higher X_c was associated with a larger P_m owing to the presence of regularly folded stems. In contrast, TraPPE-UA, PEM-CM-UA, and PEM-CVE-UA exhibited disordered globular folded structures, where relatively large P_m values were observed but X_c remained low.

Although single-chain folding crystallization provides insight into the chain conformational evolution and lamellar folding behavior, bulk polymer systems also involve cooperative effects associated with inter-chain interactions and chain packing. Therefore, the glass transition temperature (T_g) of the multi-chain PE systems was further investigated to evaluate the capability of PEM-C-UA to describe the physicochemical properties of PE. Three systems with different chain lengths, CL500, CL2000, and CL500/2000, were constructed, where CL denotes the chain length. The CL500 system consists of forty C500 chains, the CL2000 system consists of ten C2000 chains, and the mixed CL500/2000 system contains twenty C500 chains and five C2000 chains. The total number of united atoms in each system was maintained at approximately 20000. The glass transition temperatures were determined from the density-temperature relationships obtained during the cooling simulations under the NPT ensemble. As shown in Fig. 13, the simulated T_g values for the CL500, CL2000, and CL500/2000 systems are 273.3, 282.4 and 276.4 K, respectively. These values are consistent with previously reported simulation results and experimental data.[36,93,94]

To further validate the applicability of the PEM-C-UA force field for simulating crystallization in multi-chain systems, a stretching-induced crystallization approach was employed to investigate the crystallization process of PE multi-chain systems.[95–98] As shown in Fig. 14(a), different multi-chain systems were first equilibrated at 600 K under the NPT ensemble for 2 ns to ensure sufficient chain relaxation. Subsequently, the multi-chain systems were stretched along the *X*-axis direction under the NVT ensemble until the strain reached 2 at a strain rate of 10^{10} s^{-1}. After deformation, the systems were cooled to 300 K and further crystallized in the NPT ensemble for 40 ns.

Fig. 14(b) shows the evolution of the crystallinity of different multi-chain systems. The crystallinity of all systems increased rapidly in the initial stage and then remained relatively stable. The final crystallinity values of the investigated systems ranged from approximately 0.2 to 0.3, which are comparable to the crystallinity range reported for PE systems subjected to similar stretching conditions.[95] Furthermore, the CL500 system exhibits a higher final crystallinity than the CL2000 system, which can be attributed to the chain mobility and packing efficiency associated with the chain length. This chain-length-dependent crystallization behavior is consistent with previous simulation studies.[97,99] These results provide a preliminary validation of the applicability of the PEM-C-UA force field to simulate the crystallization behavior of multi-chain systems and further support its application in bulk systems crystallization simulations.

To ensure the computational efficiency of the proposed UA model, we compared the UA and AA models using single PE chains of different chain lengths. The MD simulations were performed at 600 K for 1 ns, followed by 300 K for 5 ns. For each system, three independent simulations were performed under different force fields and the average computational time was reported. Fig. 15 shows the computational time per step as a function of the number of carbon atoms using different force fields. The computational time per step of the UA model was consistently lower than that of the OPLS-AA model, and the computational cost difference became increasingly pronounced with increasing chain length. The per-step computational time of PEM-C-UA lies between those of TraPPE-UA and OPLS-UA, indicating comparable computational efficiency to that of conventional UA force fields.

Potential Energy Compensation in UA Modeling

To elucidate the potential energy compensation behavior underlying the improved performance of the UA model developed in this study, an energy comparison with the OPLS-AA force field was performed. The energy change ΔE is the difference between the energy of each UA force field and the OPLS-AA ($\Delta E = E^{UA} - E^{AA}$). The potential energy E is decomposed into E_{bonded} and $E_{non\text{-}bonded}$.

https://doi.org/10.1007/s10118-026-3889-x

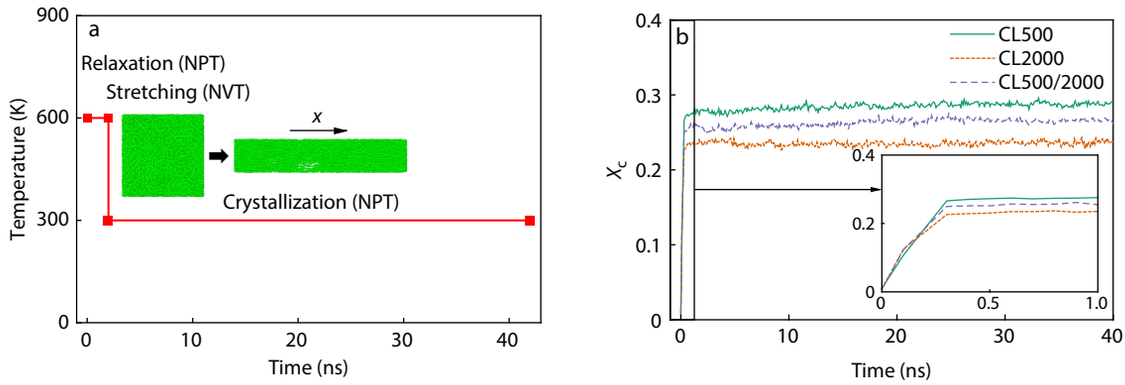


Fig. 14 Scheme of stretch-induced crystallization of multi-chain systems and the time evolution of crystallinity: (a) scheme of stretch-induced crystallization, (b) time evolution of crystallinity for different multi-chain systems using PEM-C-UA.

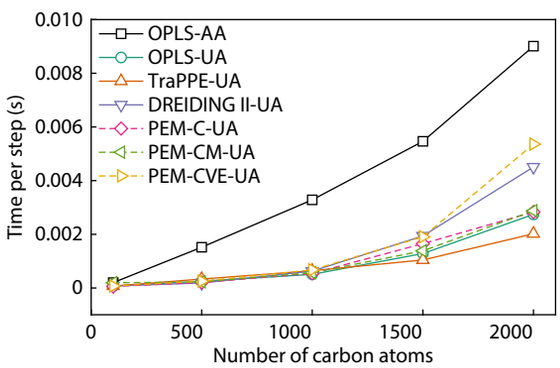


Fig. 15 Comparison of computational time per step as a function of the number of carbon atoms using different force fields.

Fig. 16 presents energy change of folded chains under various force fields after isothermal and non-isothermal crystallization. It can be seen that energy change of folded chains with different lengths exhibit similar patterns. ΔE_{bond} and ΔE_{angle} for all UA force fields are negative and nearly identical. This inevitable energy loss results from the UA simplification, which neglects hydrogen atoms. $\Delta E_{dihedral}$ are negative for OPLS-UA, while they are close to zero for TraPPE-UA and DREIDING II-UA. In contrast, $\Delta E_{dihedral}$ are significantly above zero for the UA force fields developed in this work. ΔE_{LJ} are close to zero for most force fields, except for DREIDING II-UA, which is below zero. Overall, $\Delta E_{potential}$ for the three conventional UA force fields are significantly below zero, whereas the UA force fields developed maintain $\Delta E_{potential}$ close to zero. This is primarily due to the sum ΔE_{bond}, ΔE_{angle}, and $\Delta E_{dihedral}$ within the bonded interactions.

To quantify the effect of energy losses in E_{bond} and E_{angle} and the energy increase in $E_{dihedral}$ for the UA force fields developed, the change in the bonded interactions ΔE_{bonded} was calculated and normalized by the number of beads in the UA chain. Table 3 shows ΔE_{bonded} per bead after IC and NIC under different force fields. The absolute values of ΔE_{bonded} per bead for the developed UA force fields were significantly lower than those for conventional UA force fields. It is evident that PEM-C-UA exhibits the smallest absolute value of ΔE_{bonded} per bead among all the UA force fields. After IC, ΔE_{bonded} per atom of C500 was 0.173 kcal/mol for PEM-C-UA and −3.150 kcal/mol for OPLS-UA. Both IC and NIC led to a similar ΔE_{bonded} per bead of the folded chains. ΔE_{bonded} per bead for PEM-C-UA did not exceed 0.2 kcal/mol. Under PEM-C-UA, the energy increase in $\Delta E_{dihedral}$ effectively compensated for the energy losses in E_{bond} and E_{angle}.

To ensure that ΔE_{bonded} is in good agreement with the AA model based on potential energy matching, the dihedral torsional barriers were enhanced to compensate for the energy losses in bond stretching and angle bending during UA modeling. The UA force field, PEM-C-UA, accurately reproduced the chain folding and crystallization observed in AA simulations, with this high accuracy attributed to potential energy compensation. In addition, this compensation strategy provides clear guidance for introducing improper torsional angle potentials to optimize the UA model[45,55] for which parameter modifications are introduced arbitrarily. It should be noted that such potential energy redistribution may not be limited to PE. Similar adjustments of dihedral torsional potentials have also been reported for polypropylene (PP) to improve the description of the chain conformational behavior in UA models.[45] However, the specific compensation strategy may vary depending on the molecular architecture and local interaction characteristics of different polymers, and further validation is required for other polymer systems.

More generally, the observed potential energy compensation arises from the redistribution of energetic contributions associated with the reduction in the degrees of freedom during UA modeling. By removing explicit hydrogen atoms, the UA models inevitably reduce the degrees of freedom and influence the configurational entropy of the system. Although rigorous CG potentials can be derived from free-energy-based approaches, such as the potential of mean force (PMF), the objective of the present potential energy matching approach is to preserve the potential energy characteristics and conformational energetics of the OPLS-AA model. The redistribution of energetic contributions induced by the reduction in degrees of freedom was effectively captured through the optimization of the relevant potential terms. Therefore, PEM-C-UA provides an energetically consistent representation of the PE conformational behavior. For applications involving more complex thermodynamic properties, where entropy contributions play a dominant role, further incorporation of free-energy-based corrections may be considered.

https://doi.org/10.1007/s10118-026-3889-x

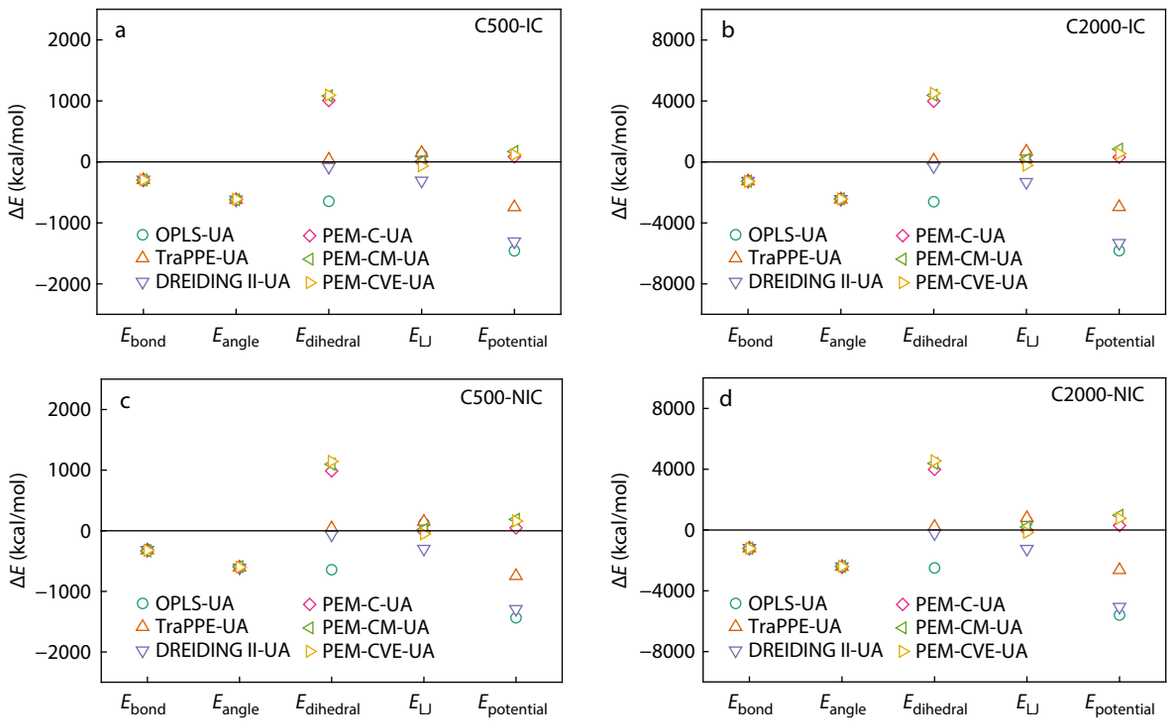


Fig. 16 Energy change of folded chains after IC and NIC under different force fields. (a) C500-IC, (b) C2000-IC, (c) C500-NIC, (d) C2000-NIC.

Table 3 ΔE_{bonded} per bead of C500 and C2000 after IC and NIC under different force fields.

Force field	ΔE_{bonded}			
	C500-IC	C2000-IC	C500-NIC	C2000-NIC
OPLS-UA	−3.150	−3.166	−3.116	−3.064
TraPPE-UA	−1.781	−1.823	−1.793	−1.712
DREIDING II-UA	−1.992	−1.996	−1.986	−1.902
PEM-C-UA	0.173	0.134	0.122	0.166
PEM-CM-UA	0.321	0.338	0.331	0.381
PEM-CVE-UA	0.361	0.386	0.430	0.463

CONCLUSIONS

A bottom-up UA model for PE was developed based on a potential energy matching approach using MD simulations. The reference potential energies of the CH_n groups were initially determined *via* atomistic simulations using the OPLS-AA force field. The parameterization of the UA model was conducted using the trajectories of PE chains. The effectiveness of constructing a UA model with carbon atoms as the mapping interaction centers, rather than centers of mass or centers of valence electrons, was demonstrated from the perspective of the potential energy. The calculation results show that the PEM-C-UA force field, using carbon atoms as the mapping centers, exhibits minimal error in predicting the bonded energy among various UA force fields. This improved performance may be attributed to the direct preservation of the carbon backbone topology, which provides a more physically consistent representation of the structural framework governing the PE conformational behavior.

In addition, PEM-C-UA can successfully reproduce the folding behavior of a single PE chain, exhibiting accuracy and reliability in good agreement with those of OPLS-AA under both isothermal and non-isothermal conditions. In PEM-C-UA, a single chain forms a regularly folded stem, consistent with OPLS-AA, whereas other UA force fields produce disordered, globular folded structures. The crystallinities of the folded stems obtained using PEM-C-UA are in good agreement with those obtained using OPLS-AA. PE chains crystallize synchronously under both the PEM-C-UA and OPLS-AA force fields during isothermal crystallization, whereas crystallization occurs earlier under PEM-C-UA than under OPLS-AA in non-isothermal crystallization. Furthermore, the PEM-C-UA force field can effectively reproduce the glass transition characteristics and crystallization behavior of PE multi-chain systems, providing preliminary validation of its applicability to multi-chain systems.

The improvement in the UA model developed in this study mainly lies in the implementation of compensation for potential energy. In the UA model, the hydrogen atoms present in the AA model are omitted, which results in inevitable energy losses during bond stretching and angle bending. The dihedral torsion energy increases, leading to higher energy barriers for dihedral rotation and effective compensation for the energy losses in bond stretching and angle bending. This ensures that the bonded interactions and potential energy un-

https://doi.org/10.1007/s10118-026-3889-x

der PEM-C-UA are in good agreement with those of OPLS-AA. Overall, this study proposes a potential energy-matching UA modeling approach and validates its applicability, providing a UA force field for PE MD simulations.

Conflict of Interests

The authors declare no interest conflict.

Data Availability Statement

The related data of this paper can be obtained from the author for reasonable reasons. The author's contact information: miaocq@hit.edu.cn (C.Q.M.).

REFERENCES

1 Schwab, S. T.; Baur, M.; Nelson, T. F.; Mecking, S. Synthesis and deconstruction of polyethylene-type materials. *Chem. Rev.* **2024**, *124*, 2327−2351.
2 Olesik, P.; Godzierz, M.; Kozioł, M.; Jała, J.; Szeluga, U.; Myalski, J. Structure and mechanical properties of high-density polyethylene composites reinforced with glassy carbon. *Materials* **2021**, *14*, 4024.
3 Tan, C.; Zou, C.; Chen, C. Material properties of functional polyethylenes from transition-metal-catalyzed ethylene–polar monomer copolymerization. *Macromolecules* **2022**, *55*, 1910−1922.
4 Mahmood, Q.; Hu, Z.; Ren, G.; Sun, W. H. Recent advances in nickel catalysis for thermoplastic polyethylene elastomers: synthesis strategies, properties, and future perspectives. *Coord. Chem. Rev.* **2025**, *541*, 216833.
5 Jordan, J. L.; Casem, D. T.; Bradley, J. M.; Dwivedi, A. K.; Brown, E. N.; Jordan, C. W. Mechanical properties of low density polyethylene. *J. Dyn. Behav. Mater.* **2016**, *2*, 411−420.
6 Patel, K.; Chikkali, S. H.; Sivaram, S. Ultrahigh molecular weight polyethylene: catalysis, structure, properties, processing and applications. *Prog. Polym. Sci.* **2020**, *109*, 101290.
7 Kanagaraj, S.; Varanda, F. R.; Zhil'tsova, T. V.; Oliveira, M. S. A.; Simões, J. A. O. Mechanical properties of high density polyethylene/carbon nanotube composites. *Compos. Sci. Technol.* **2007**, *67*, 3071−3077.
8 Fouad, H.; Elleithy, R.; Al-Zahrani, S. M.; Ali, M. A. Characterization and processing of high density polyethylene/carbon nano-composites. *Mater. Des.* **2011**, *32*, 1974−1980.
9 Walker, T. W.; Frelka, N.; Shen, Z.; Chew, A. K.; Banick, J.; Grey, S.; Kim, M. S.; Dumesic, J. A.; Van Lehn, R. C.; Huber, G. W. Recycling of multilayer plastic packaging materials by solvent-targeted recovery and precipitation. *Sci. Adv.* **2020**, *6*, eaba7599.
10 Sadler, D. M.; Keller, A. Neutron scattering studies on the molecular trajectory in polyethylene crystallized from solution and melt. *Macromolecules* **1977**, *10*, 1128−1140.
11 Zeng, X.; Ungar, G.; Spells, S. J.; King, S. M. Real-time neutron scattering study of transient phases in polymer crystallization. *Macromolecules* **2005**, *38*, 7201−7204.
12 Reddy, K. R.; Tashiro, K.; Sakurai, T.; Yamaguchi, N. Cocrystallization phenomenon between the H and D species of isotactic polypropylene blends as revealed by thermal and infrared spectroscopic analyses for a series of D/H blend samples. *Macromolecules* **2008**, *41*, 9807−9813.
13 Mizushima, M.; Kawamura, T.; Takahashi, K.; Nitta, K. H. Characterization of molecular orientation under tensile deformation by near infrared spectroscopy. *E-Polymers* **2012**, *12*, 68.
14 Al-Raheil, I. A. M.; Okaz, A. M. Chain-folding in polyethylene lamellar structure. *Polym. Int.* **1992**, *28*, 261−263.
15 Miao, J.; Cui, L.; Lau, H. P.; Mather, P. T.; Zhu, L. Self-assembly and chain-folding in hybrid coil–coil–cube triblock oligomers of polyethylene-*b*-poly(ethylene oxide)-*b*-polyhedral oligomeric silsesquioxane. *Macromolecules* **2007**, *40*, 5460−5470.
16 Ma, Z.; Yang, P.; Zhang, X.; Jiang, K.; Song, Y.; Zhang, W. Quantifying the chain folding in polymer single crystals by single-molecule force spectroscopy. *ACS Macro Lett.* **2019**, *8*, 1194−1199.
17 Song, Y.; Ma, Z.; Yang, P.; Zhang, X.; Lyu, X.; Jiang, K.; Zhang, W. Single-molecule force spectroscopy study on force-induced melting in polymer single crystals: the chain conformation matters. *Macromolecules* **2019**, *52*, 1327−1333.
18 Hong, Y. L.; Miyoshi, T. Elucidation of the chain-folding structure of a semicrystalline polymer in single crystals by solid-state NMR. *ACS Macro Lett.* **2014**, *3*, 556−559.
19 Luo, X.; Xie, S. J.; Huang, W.; Dai, B. N.; Lu, Z. Y.; Yan, D. Y. Effect of branching architecture on glass transition behavior of hyperbranched copolystyrenes: the experiment and simulation studies. *Chinese J. Polym. Sci.* **2016**, *34*, 77−87.
20 Dewapriya, M. A. N.; Gillespie Jr, J. W.; Deitzel, J. M. Exploring the effects of temperature, transverse pressure, and strain rate on axial tensile behavior of perfect UHMWPE crystals using molecular dynamics. *Compos. Part B Eng.* **2025**, *294*, 112160.
21 Venkatesan, S.; Basu, S. Investigations into crazing in glassy amorphous polymers through molecular dynamics simulations. *J. Mech. Phys. Solids* **2015**, *77*, 123−145.
22 Wang, J.; Zhu, X.; Lu, X.; Zhou, Z.; Wang, G. On structures and properties of polyethylene during heating and cooling processes based on molecular dynamics simulations. *Comput. Theor. Chem.* **2015**, *1052*, 26−34.
23 Chremos, A.; Douglas, J. F. Influence of branching on the configurational and dynamical properties of entangled polymer melts. *Polymers* **2019**, *11*, 1045.
24 Lin, H.; Erguney, F.; Mattice, W. L. Collapsed chains as models for filler particles in a polymer melt. *Polymer* **2005**, *46*, 6154−6162.
25 Ramos, J.; Vega, J. F.; Theodorou, D. N.; Martinez-Salazar, J. Entanglement relaxation time in polyethylene: simulation versus experimental data. *Macromolecules* **2008**, *41*, 2959−2962.
26 Kos, P. I.; Ivanov, V. A.; Chertovich, A. V. Crystallization of semiflexible polymers in melts and solutions. *Soft Matter* **2021**, *17*, 2392−2403.
27 Boudaghi, M.; Edwards, B. J.; Khomami, B. Microstructural evolution and reverse flow in shear-banding of entangled polymer melts. *Soft Matter* **2023**, *19*, 410−429.
28 Marrink, S. J.; Risselada, H. J.; Yefimov, S.; Tieleman, D. P.; de Vries, A. H. The MARTINI force field: coarse grained model for biomolecular simulations. *J. Phys. Chem. B* **2007**, *111*, 7812−7824.
29 Padding, J. T.; Briels, W. J. Time and length scales of polymer melts studied by coarse-grained molecular dynamics simulations. *J. Chem. Phys.* **2002**, *117*, 925−943.
30 Edwards, B. J.; Nafar Sefiddashti, M. H.; Khomami, B. Atomistic simulation of shear flow of linear alkane and polyethylene liquids: a 50-year retrospective. *J. Rheol.* **2022**, *66*, 415−489.
31 Noid, W. G. Perspective: coarse-grained models for biomolecular systems. *J. Chem. Phys.* **2013**, *139*, 090901.
32 Moore, T. C.; Iacovella, C. R.; McCabe, C. Derivation of coarse-grained potentials *via* multistate iterative Boltzmann inversion. *J. Chem. Phys.* **2014**, *140*, 224104.
33 Sgouros, A. P.; Megariotis, G.; Theodorou, D. N. Slip-spring model for the linear and nonlinear viscoelastic properties of molten polyethylene derived from atomistic simulations.

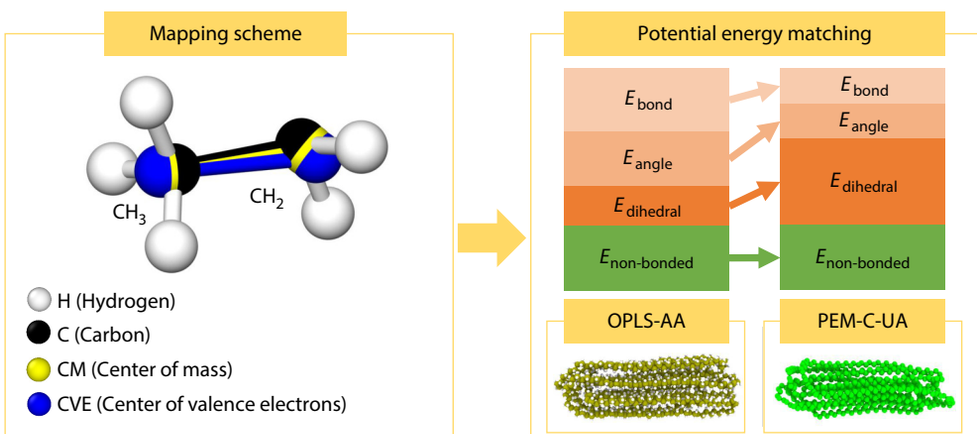
Graphical Abstract

A Bottom-up United-atom Model for Polyethylene Chain Crystallization: a Potential Energy Matching Approach

Jing-Fu Shi, Di Song, Lei Liu, and Chang-Qing Miao

Harbin Institute of Technology; University of Electronic Science and Technology of China

This study developed a bottom-up united-atom (UA) model for polyethylene (PE) chain crystallization based on potential energy matching, demonstrated the effectiveness of carbon atoms as mapping centers, and revealed that dihedral energy compensation maintains energy consistency and reproduces chain conformational evolution comparable to that of optimized potentials for liquid simulations–all atom (OPLS-AA) simulations.



Chinese J. Polym. Sci. 2026 *https://doi.org/10.1007/s10118-026-3889-x*

Macromolecules **2017**, *50*, 4524–4541.
34 Joshi, S. Y.; Deshmukh, S. A. A review of advancements in coarse-grained molecular dynamics simulations. *Mol. Simul.* **2021**, *47*, 786–803.
35 Shen, H.; Li, Y.; Ren, P.; Zhang, D.; Li, G. Anisotropic coarse-grained model for proteins based on gay–berne and electric multipole potentials. *J. Chem. Theory Comput.* **2014**, *10*, 731–750.
36 Hossain, D.; Tschopp, M. A.; Ward, D. K.; Bouvard, J. L.; Wang, P.; Horstemeyer, M. F. Molecular dynamics simulations of deformation mechanisms of amorphous polyethylene. *Polymer* **2010**, *51*, 6071–6083.
37 Kim, J. M.; Locker, R.; Rutledge, G. C. Plastic deformation of semicrystalline polyethylene under extension, compression, and shear using molecular dynamics simulation. *Macromolecules* **2014**, *47*, 2515–2528.
38 Shi, J.; Zhou, J.; Liu, L.; Liu, W.; Miao, C. Molecular dynamic simulations of deformation behaviour of blended polyethylene. *Mol. Simul.* **2023**, *49*, 1698–1708.
39 Jorgensen, W. L.; Madura, J. D.; Swenson, C. J. Optimized intermolecular potential functions for liquid hydrocarbons. *J. Am. Chem. Soc.* **1984**, *106*, 6638–6646.
40 Wick, C. D.; Martin, M. G.; Siepmann, J. I. Transferable potentials for phase equilibria. 4. united-atom description of linear and branched alkenes and alkylbenzenes. *J. Phys. Chem. B* **2000**, *104*, 8008–8016.
41 Mayo, S. L.; Olafson, B. D.; Goddard, W. A. DREIDING: a generic force field for molecular simulations. *J. Phys. Chem.* **1990**, *94*, 8897–8909.
42 Paul, W.; Yoon, D. Y.; Smith, G. D. An optimized united atom model for simulations of polymethylene melts. *J. Chem. Phys.* **1995**, *103*, 1702–1709.
43 Nath, S. K.; Escobedo, F. A.; de Pablo, J. J. On the simulation of vapor–liquid equilibria for alkanes. *J. Chem. Phys.* **1998**, *108*, 9905–9911.
44 Li, C.; Choi, P.; Sundararajan, P. R. Simulation of chain folding in polyethylene: a comparison of united atom and explicit hydrogen atom models. *Polymer* **2010**, *51*, 2803–2808.
45 Hagita, K.; Fujiwara, S. Single-chain folding of a quenched isotactic polypropylene chain through united atom molecular dynamics simulations. *Polymer* **2019**, *183*, 121861.
46 Shi, J.; Zhou, J.; Liu, L.; Miao, C. Molecular dynamics simulations of single polyethylene chain folding during fast quenching using all-atom and united-atom models. *Phys. Chem. Chem. Phys.* **2024**, *26*, 24995–25004.
47 Jiang, S.; Lu, Y.; Luo, C. State transitions and crystalline structures of a single polyethylene chain: MD simulations. *J. Phys. Chem. B* **2022**, *126*, 964–975.
48 Shi, J.; Song, D.; Liu, L.; Miao, C. Folding behavior of polyethylene chains with different topologies: insights from all-atom and united-atom simulations. *J. Macromol. Sci. Part B* **2026**, 1–17.
49 Jorgensen, W. L.; Maxwell, D. S.; Tirado-Rives, J. Development and testing of the OPLS all-atom force field on conformational energetics and properties of organic liquids. *J. Am. Chem. Soc.* **1996**, *118*, 11225–11236.

50 Hussain, M. A.; Yamamoto, T.; Adil, S. F.; Yao, S. Preparation and characterization of high-density polyethylene with alternating lamellar stems using molecular dynamics simulations. *Polymers* **2024**, *16*, 304.
51 Hussain, M. A.; Yamamoto, T.; Adil, S. F.; Yao, S. Coarse-grained simulations on polyethylene crystal network formation and microstructure analysis. *Polymers* **2024**, *16*, 1007.
52 Hagita, K.; Fujiwara, S.; Iwaoka, N. Structure formation of a quenched single polyethylene chain with different force fields in united atom molecular dynamics simulations. *AIP Adv.* **2018**, *8*, 115108.
53 Olsson, P. A. T.; Schröder, E.; Hyldgaard, P.; Kroon, M.; Andreasson, E.; Bergvall, E. Ab initio and classical atomistic modelling of structure and defects in crystalline orthorhombic polyethylene: twin boundaries, slip interfaces, and nature of barriers. *Polymer* **2017**, *121*, 234–246.
54 Olsson, P. A. T.; in 't Veld, P. J.; Andreasson, E.; Bergvall, E.; Persson Jutemar, E.; Petersson, V.; Rutledge, G. C.; Kroon, M. All-atomic and coarse-grained molecular dynamics investigation of deformation in semi-crystalline lamellar polyethylene. *Polymer* **2018**, *153*, 305–316.
55 Sundararajan, P. R.; Kavassalis, T. A. Molecular dynamics study of polyethylene chain folding: the effects of chain length and the torsional barrier. *Faraday Trans.* **1995**, *91*, 2541.
56 Pütz, M.; Curro, J. G.; Grest, G. S. Self-consistent integral equation theory for polyolefins: comparison to molecular dynamics simulations and X-ray scattering. *J. Chem. Phys.* **2001**, *114*, 2847–2860.
57 Yamamoto, T.; Sawada, K. Molecular-dynamics simulation of crystallization in helical polymers. *J. Chem. Phys.* **2005**, *123*, 234906.
58 Yamamoto, T. Molecular dynamics of crystallization in a helical polymer isotactic polypropylene from the oriented amorphous state. *Macromolecules* **2014**, *47*, 3192–3202.
59 McCoy, J. D.; Curro, J. G. Mapping of explicit atom onto united atom potentials. *Macromolecules* **1998**, *31*, 9362–9368.
60 Toxvaerd, S. Molecular dynamics calculation of the equation of state of alkanes. *J. Chem. Phys.* **1990**, *93*, 4290–4295.
61 Toxvaerd, S. Equation of state of alkanes II. *J. Chem. Phys.* **1997**, *107*, 5197–5204.
62 Biscay, F.; Ghoufi, A.; Goujon, F.; Lachet, V.; Malfreyt, P. Surface tensions of linear and branched alkanes from Monte Carlo simulations using the anisotropic united atom model. *J. Phys. Chem. B* **2008**, *112*, 13885–13897.
63 Biscay, F.; Ghoufi, A.; Lachet, V.; Malfreyt, P. Calculation of the surface tension of cyclic and aromatic hydrocarbons from Monte Carlo simulations using an anisotropic united atom model (AUA). *Phys. Chem. Chem. Phys.* **2009**, *11*, 6132–6147.
64 Anaya, L. E. C.; Gómez, S. Y.; Orozco, G. A. Comprehensive automated routine implementation, validation, and benchmark of the anisotropic force field (AUA4) using Python and GROMACS. *J. Phys. Chem. A* **2023**, *127*, 1555–1563.
65 Marrink, S. J.; Tieleman, D. P. Perspective on the martini model. *Chem. Soc. Rev.* **2013**, *42*, 6801–6822.
66 Tanis, I.; Rousseau, B.; Soulard, L.; Lemarchand, C. A. Assessment of an anisotropic coarse-grained model for *cis*-1, 4-polybutadiene: a bottom-up approach. *Soft Matter* **2021**, *17*, 621–636.
67 Salerno, K. M.; Agrawal, A.; Perahia, D.; Grest, G. S. Resolving dynamic properties of polymers through coarse-grained computational studies. *Phys. Rev. Lett.* **2016**, *116*, 058302.
68 Peters, B. L.; Salerno, K. M.; Agrawal, A.; Perahia, D.; Grest, G. S. Coarse-grained modeling of polyethylene melts: effect on dynamics. *J. Chem. Theory Comput.* **2017**, *13*, 2890–2896.
69 Nguyen, H. T. L.; Huang, D. M. Systematic bottom-up molecular coarse-graining *via* force and torque matching using anisotropic particles. *J. Chem. Phys.* **2022**, *156*, 184118.
70 Wilson, M. O.; Huang, D. M. Anisotropic molecular coarse-graining by force and torque matching with neural networks. *J. Chem. Phys.* **2023**, *159*, 024110.
71 Kempfer, K.; Devémy, J.; Dequidt, A.; Couty, M.; Malfreyt, P. Development of coarse-grained models for polymers by trajectory matching. *ACS Omega* **2019**, *4*, 5955–5967.
72 Kempfer, K.; Devémy, J.; Dequidt, A.; Couty, M.; Malfreyt, P. Multi-scale modeling of the polymer–filler interaction. *Soft Matter* **2020**, *16*, 1538–1547.
73 Campos-Villalobos, G.; Giunta, G.; Marín-Aguilar, S.; Dijkstra, M. Machine-learning effective many-body potentials for anisotropic particles using orientation-dependent symmetry functions. *J. Chem. Phys.* **2022**, *157*, 024902.
74 DelloStritto, M.; Klein, M. L. Understanding strain and failure of a knot in polyethylene using molecular dynamics with machine-learned potentials. *J. Phys. Chem. Lett.* **2024**, *15*, 9070–9077.
75 Liu, L.; Zhou, J.; Shi, J.; Miao, C. The mechanical anisotropy and failure mechanism of poly(*p*-phenylene terephthalamide) using machine learning molecular dynamics simulations. *Macromolecules* **2024**, *57*, 6941–6953.
76 Wang, J.; Olsson, S.; Wehmeyer, C.; Pérez, A.; Charron, N. E.; de Fabritiis, G.; Noé, F.; Clementi, C. Machine learning of coarse-grained molecular dynamics force fields. *ACS Cent. Sci.* **2019**, *5*, 755–767.
77 Yue, T.; He, J.; Tao, L.; Li, Y. High-throughput screening and prediction of high modulus of resilience polymers using explainable machine learning. *J. Chem. Theory Comput.* **2023**, *19*, 4641–4653.
78 Tang, P. H.; Chen, P. H.; Li, F. C.; Lu, C. H.; Huang, C. I.; Pao, C. W. Multiscale molecular simulations of the morphological evolution of small-molecule organic solar cells during the vacuum codeposition process. *Phys. Rev. Materials* **2020**, *4*, 095601.
79 Hansen, N.; Müller, S. D.; Koumoutsakos, P. Reducing the time complexity of the derandomized evolution strategy with covariance matrix adaptation (CMA-ES). *Evol. Comput.* **2003**, *11*, 1–18.
80 Hansen, N.; Ostermeier, A. Completely derandomized self-adaptation in evolution strategies. *Evol. Comput.* **2001**, *9*, 159–195.
81 Plimpton, S. Fast parallel algorithms for short-range molecular dynamics. *J. Comput. Phys.* **1995**, *117*, 1–19.
82 Nosé, S. A unified formulation of the constant temperature molecular dynamics methods. *J. Chem. Phys.* **1984**, *81*, 511–519.
83 Hoover, W. G. Canonical dynamics: equilibrium phase-space distributions. *Phys. Rev. A* **1985**, *31*, 1695–1697.
84 Hur, K.; Jeong, C.; Winkler, R. G.; Lacevic, N.; Gee, R. H.; Yoon, D. Y. Chain dynamics of ring and linear polyethylene melts from molecular dynamics simulations. *Macromolecules* **2011**, *44*, 2311–2315.
85 Dimitrov, D. I.; Milchev, A.; Binder, K.; Klushin, L. I.; Skvortsov, A. M. Universal properties of a single polymer chain in slit: scaling versus molecular dynamics simulations. *J. Chem. Phys.* **2008**, *128*, 234902.
86 Zhang, X.; Bhatt, D.; Zuckerman, D. M. Automated sampling assessment for molecular simulations using the effective sample size. *J. Chem. Theory Comput.* **2010**, *6*, 3048–3057.
87 Olowookere, F. V.; Al Alshaikh, A.; Bara, J. E.; Turner, C. H. Effects of chain length on the structure and dynamics of polyvinyl chloride during atomistic molecular dynamics simulations. *Mol. Simul.* **2023**, *49*, 1401–1412.
88 Frau, M.; Tarabunga, P. S.; Collura, M.; Dalmonte, M.; Tirrito, E. Nonstabilizerness versus entanglement in matrix product states. *Phys. Rev. B* **2024**, *110*, 045101.

https://doi.org/10.1007/s10118-026-3889-x

89 Nafar Sefiddashti, M. H.; Edwards, B. J.; Khomami, B. Individual chain dynamics of a polyethylene melt undergoing steady shear flow. *J. Rheol.* **2015**, *59*, 119–153.
90 Afzal, M. A. F.; Browning, A. R.; Goldberg, A.; Halls, M. D.; Gavartin, J. L.; Morisato, T.; Hughes, T. F.; Giesen, D. J.; Goose, J. E. High-throughput molecular dynamics simulations and validation of thermophysical properties of polymers for various applications. *ACS Appl. Polym. Mater.* **2021**, *3*, 620–630.
91 Yu, X.; Kong, B.; Yang, X. Molecular dynamics study on the crystallization of a cluster of polymer chains depending on the initial entanglement structure. *Macromolecules* **2008**, *41*, 6733–6740.
92 Hu, Y.; Shao, Y.; Liu, Z.; He, X.; Liu, B. Dominant effects of short-chain branching on the initial stage of nucleation and formation of Tie chains for bimodal polyethylene as revealed by molecular dynamics simulation. *Polymers* **2019**, *11*, 1840.
93 Song, J.; Li, J.; Li, Z. Molecular dynamics simulations of uniaxial deformation of bimodal polyethylene melts. *Polymer* **2021**, *213*, 123210.
94 Davis, G. T.; Eby, R. K. Glass transition of polyethylene: volume relaxation. *J. Appl. Phys.* **1973**, *44*, 4274–4281.
95 Liu, Z.; Zhou, Z.; Ming, Y.; Zhang, S.; Hao, T.; Nie, Y. Molecular dynamics simulations of nucleation details in stretched polyethylene. *Polymer* **2020**, *195*, 122442.
96 Lavine, M. S.; Waheed, N.; Rutledge, G. C. Molecular dynamics simulation of orientation and crystallization of polyethylene during uniaxial extension. *Polymer* **2003**, *44*, 1771–1779.
97 Grommes, D.; Schenk, M. R.; Bruch, O.; Reith, D. Investigation of crystallization and relaxation effects in coarse-grained polyethylene systems after uniaxial stretching. *Polymers* **2021**, *13*, 4466.
98 Kearns, K. L.; Scherzer, J.; Chyasnavichyus, M.; Monaenkova, D.; Moore, J.; Sammler, R. L.; Fielitz, T.; Nicholson, D. A.; Andreev, M.; Rutledge, G. C. Measuring flow-induced crystallization kinetics of polyethylene after processing. *Macromolecules* **2021**, *54*, 2101–2112.
99 Triandafilidi, V.; Rottler, J.; Hatzikiriakos, S. G. Molecular dynamics simulations of monodisperse/bidisperse polymer melt crystallization. *J. Polym. Sci. Part B Polym. Phys.* **2016**, *54*, 2318–2326.

https://doi.org/10.1007/s10118-026-3889-x